

Splintering central nuclear collisions with a momentum-dependent lattice Hamiltonian theory

Declan Persram and Charles Gale

Physics Department, McGill University

3600 University St., Montréal, QC, H3A 2T8, Canada

(June 17, 2021)

Abstract

We formulate a lattice Hamiltonian model for intermediate energy heavy ion collisions. Our approach incorporates a momentum-dependent nuclear mean field that yields an optical potential that agrees with proton-nucleus experiments and that also receives support from measurements involving heavy ions. We emphasize the precision of our numerical results in connection with energy and momentum conservation. We first outline the static properties of our solutions, after which we consider recent stopping power results for heavy ion collisions. The results obtained with different types of nuclear mean fields are compared with each other. Consequences of the stopping power data on the determination of the nuclear equation of state are outlined.

PACS : 24.10.-i, 25.70.Jj, 25.70.Pq

I. INTRODUCTION

Heavy ion collisions remain the only practical area of research which addresses the physics of strongly interacting matter in states far away from equilibrium. As such, it represents a rich and challenging field well worthy of intellectual pursuit and is fundamental to a deeper and a more complete understanding of Nature. At high energies, a goal of this program is to form and study a new state of matter which is a prediction of QCD: the quark-gluon plasma [1]. At lower energies, the experimental and theoretical efforts have focused on the need to characterize and quantify the nuclear equation of state [2]. This physics also has an important role to play in the theory of supernovæ and that of neutron star properties [3]. It is that energy regime that we consider in this work.

A popular practice consists of characterizing the nuclear equation of state in terms of its coefficient of compressibility, K . This number can be deduced from Hartree-Fock-plus-RPA analyses of giant monopole resonances in finite nuclei [4]. In heavy ions, in order to identify novel many-body features without ambiguity it is imperative to provide a realistic model of the nuclear reaction dynamics. An approach that has proven to be extremely successful is the Boltzmann-Uehling-Uhlenbeck (BUU) model of heavy ion collisions [5]. In BUU simulations, nucleons can suffer two-body collisions and can also move on curved trajectories owing to interactions with the self-consistent mean field. The interaction we use in this work is described in Refs. [6,7]. A large body of work in intermediate energy nuclear collisions has been devoted to the measurement and to the theoretical calculation of nuclear flow [8–11]. In connection with this observable, it is fair to state that at present little compelling evidence exists from intermediate energy heavy ion data to suggest that the value of K derived from heavy ion collisions [7] should be different from that inferred from recent giant monopole studies [12]. Both methods of analysis suggested $K \approx 215$ MeV. However, a recent study can be found in Ref. [13].

Near the low end of the intermediate energy spectrum, some studies have put forward the possibility of observing experimental signatures of new phenomena. A good example is that of reduced in-medium nucleon-nucleon cross sections [14–17]. While the confirmation of such manifestations would indeed be extremely interesting, one must keep in mind that such “new physics” issues must be addressed with an approach that incorporates all of the known physics in a computationally tractable model. Our goal in this paper is to present such a model. At beam energies such as the ones under consideration in this work, the problem of energy and momentum conservation in transport models is a pressing one. Also, it is of course necessary to include the Coulomb interaction for adequate phenomenology. Finally, the momentum dependence of the nuclear mean field is an unavoidable feature, both from the point of view of theory [18,19] as from that of experiment [20,21]. Those elements are incorporated in our model. The conservation law requirements vital in this low energy environment are enforced via the Lattice Hamiltonian algorithm [22].

Our paper is organized as follows: the next section introduces our Lattice Hamiltonian. The following section explores its static solutions. We then proceed to a discussion of the Vlasov limit of our transport theory, followed by a full BUU analysis. We apply our model to a specific measurement of stopping power in nuclear collisions. We close with a summary and conclusion.

II. LATTICE HAMILTONIAN

We wish to solve the equations of motion for a system of particles interacting via a self-consistent mean field potential. The first step in our numerical solution is to write down the Hamiltonian for a system of particles embedded in a six dimensional lattice $(\delta x, \delta p)$ in configuration and momentum space. The phase space distribution function of a single particle (Roman index “ i ”) located at configuration (momentum) space lattice site α (π) is

$$f_{\alpha\pi}^i = R(\vec{r}_\alpha - \vec{r}_i)P(\vec{p}_\pi - \vec{p}_i). \quad (2.1)$$

In the above, R (P) is the configuration (momentum) space form factor which we will specify shortly. If we simultaneously consider N_{ens} such systems and wish our distribution function to represent the average of these systems, then the distribution function must be normalized such that

$$(\delta x)^3(\delta p)^3 \sum_{\alpha\pi} f_{\alpha\pi}^i = N_{ens}^{-1}. \quad (2.2)$$

We define a “test particle” as one of the particles from the N_{ens} systems defined above. Note that summing the left hand side of Eq. 2.2 over “ i ”, one obtains the total number of nucleons: the proper normalization. Now before we can write down the total Hamiltonian, we need a form for the potential energy density. One choice used for heavy ion calculations which takes into account non local mean field effects is known as the MDYI potential [6]. This interaction yields good bulk nuclear matter and optical potential properties [21]. It also generates successful heavy ion phenomenology [7,23]. This potential energy density reads:

$$V(\vec{r}) = \frac{A}{2} \frac{\rho(\vec{r})^2}{\rho_0} + \frac{B}{\sigma + 1} \frac{\rho(\vec{r})^{\sigma+1}}{\rho_0^\sigma} + \frac{C\Lambda^2}{\rho_0} \int \int d^3p d^3p' \frac{f(\vec{r}, \vec{p})f(\vec{r}, \vec{p}')}{\Lambda^2 + (\vec{p} - \vec{p}')^2}, \quad (2.3)$$

where f is the phase space distribution function, and ρ_0 is the density of nuclear matter. However since we are now working on a lattice, we require the discretized version of the above:

$$V_\alpha = \frac{A}{2} \frac{\rho_\alpha^2}{\rho_0} + \frac{B}{\sigma + 1} \frac{\rho_\alpha^{\sigma+1}}{\rho_0^\sigma} + \frac{C\Lambda^2}{\rho_0} (\delta p)^6 \sum_{\pi\pi'} \frac{f_{\alpha\pi} f_{\alpha\pi'}}{\Lambda^2 + (\vec{p}_\pi - \vec{p}_{\pi'})^2}. \quad (2.4)$$

The five constants A, B, C, σ and Λ in V_α were chosen to reproduce the ground state binding energy per nucleon $E/A(\rho_0) = -16$ MeV, the nuclear compressibility $K=215$ MeV, the zero pressure condition $P(\rho_0, T = 0) = 0$, and the real part of the single particle potential (see below) to satisfy $U(\rho_0, p = 0) = -75$ MeV and $U(\rho_0, p^2/2m = 300 \text{ MeV}) = 0$. Our parameters yield $U(\rho_0, p \rightarrow \infty) = 30.5$ MeV and the effective mass at the Fermi surface is $m^*/m = 0.67$. This parameter set as well as others investigated in this work are shown in Table I. Note that in the above $f_{\alpha\pi} \equiv \sum_i f_{\alpha\pi}^i$ and the configuration space density at site α is $\rho_\alpha = (\delta p)^3 \sum_\pi f_{\alpha\pi}$. The total potential energy density at site α shown in the above discretized version of V_α is due to all of the test particles. To obtain the single particle potential we must unfold the phase space distribution function from V_α . We obtain the single particle potential from the above potential energy density through the functional derivative [24]

$$U_{\alpha\pi} \equiv \frac{\delta V_\alpha}{\delta f_{\alpha\pi}} \quad (2.5)$$

$$= A \frac{\rho_\alpha}{\rho_0} + B \frac{\rho_\alpha^\sigma}{\rho_0^\sigma} + \frac{2C\Lambda^2}{\rho_0} (\delta p)^3 \sum_{\pi'} \frac{f_{\alpha\pi'}}{\Lambda^2 + (\vec{p}_\pi - \vec{p}_{\pi'})^2}. \quad (2.6)$$

Before we move any further, a simplification will be made to the lattice phase space density. We will consider the momentum space lattice to have a spacing of $\delta p = 0$; a continuum in momentum space. With this, our phase space density is

$$f_{\alpha\pi}^i = R(\vec{r}_\alpha - \vec{r}_i) \delta(\vec{p}_\pi - \vec{p}_i), \quad (2.7)$$

where R may or may not be a delta function. With this form factor, our potential energy density and single particle potential read:

$$V_\alpha = \frac{A \rho_\alpha^2}{2 \rho_0} + \frac{B}{\sigma + 1} \frac{\rho_\alpha^{\sigma+1}}{\rho_0^\sigma} + \frac{C\Lambda^2}{\rho_0} \sum_{ij} \frac{R(\vec{r}_\alpha - \vec{r}_i) R(\vec{r}_\alpha - \vec{r}_j)}{\Lambda^2 + (\vec{p}_i - \vec{p}_j)^2} \quad (2.8)$$

$$U_\alpha(\vec{p}) = A \frac{\rho_\alpha}{\rho_0} + B \frac{\rho_\alpha^\sigma}{\rho_0^\sigma} + \frac{2C\Lambda^2}{\rho_0} \sum_i \frac{R(\vec{r}_\alpha - \vec{r}_i)}{\Lambda^2 + (\vec{p} - \vec{p}_i)^2}. \quad (2.9)$$

Now from (2.2) and (2.8) we obtain the total Hamiltonian of all test particles (N_{ens} systems of A nucleons). With the Hamiltonian

$$H = \sum_j^{A \times N_{ens}} \frac{p_j^2}{2m} + N_{ens} (\delta x)^3 \sum_\alpha V_\alpha, \quad (2.10)$$

we can write down the equations of motion for the i^{th} test particle:

$$\dot{\vec{r}}_i = \nabla_{\vec{p}_i} H = \frac{\vec{p}_i}{m} + N_{ens} (\delta x)^3 \sum_\alpha R(\vec{r}_\alpha - \vec{r}_i) \nabla_{\vec{p}_i} U_\alpha(\vec{p}_i) \quad (2.11)$$

$$\dot{\vec{p}}_i = -\nabla_{\vec{r}_i} H = -N_{ens} (\delta x)^3 \sum_\alpha U_\alpha(\vec{p}_i) \nabla_{\vec{r}_i} R(\vec{r}_\alpha - \vec{r}_i). \quad (2.12)$$

Up until now we have left the exact form of the configuration space form factor unspecified. There is however a special case which we will consider. If R does not contain a delta function, then (2.11) and (2.12) give us the ‘‘Lattice Hamiltonian’’ equations of motion. Suppose however that we let $\delta x = 0$ so that we have a continuum in both configuration and momentum space. The normalized (see equation 2.2) phase space distribution function takes the following form:

$$f_{\alpha\pi}^i = N_{ens}^{-1} \delta(\vec{r}_\alpha - \vec{r}_i) \delta(\vec{p}_\pi - \vec{p}_i). \quad (2.13)$$

Now, if we insert the above into (2.11) and (2.12) we get a new set of equations of motion which read

$$\dot{\vec{r}}_i = \frac{\vec{p}_i}{m} + \nabla_{\vec{p}_i} U(\vec{r}_i, \vec{p}_i) \quad (2.14)$$

$$\dot{\vec{p}}_i = -\nabla_{\vec{r}_i} U(\vec{r}_i, \vec{p}_i). \quad (2.15)$$

For relativistic kinematics, the m above can be replaced by $\sqrt{p^2 + m^2}$. If the test particles evolve according to Hamilton's equations, their phase space density, f , will satisfy the Vlasov equation. This equation can also be identified with the time evolution of the Wigner transform of the one-body density matrix (which in turn is directly related to the many body wave function of a system of particles) [5]. It is

$$\frac{\partial}{\partial t} f(\vec{r}, \vec{p}) + \nabla_{\vec{p}} H \cdot \nabla_{\vec{r}} f(\vec{r}, \vec{p}) - \nabla_{\vec{r}} H \cdot \nabla_{\vec{p}} f(\vec{r}, \vec{p}) = 0. \quad (2.16)$$

From here on we refer to equations (2.11) and (2.12) as ‘‘LHV’’ (Lattice Hamiltonian Vlasov) and equations (2.14) and (2.15) as ‘‘TPV’’ (test particle Vlasov).

We have mentioned that (2.11) and (2.12) are the equations of motion for a phase space density without configuration space delta functions but we did not offer a specific choice for the form factor. We follow the work of Lenk and Pandharipande [22] and adopt the form factor

$$R(\vec{r}_\alpha - \vec{r}_i) = \frac{1}{N_{ens}(n\delta x)^6} g(x_\alpha - x_i) g(y_\alpha - y_i) g(z_\alpha - z_i) \quad (2.17)$$

$$g(x_\alpha - x_i) \equiv (n\delta x - |x_\alpha - x_i|) \Theta(n\delta x - |x_\alpha - x_i|). \quad (2.18)$$

The normalization condition (2.2) is satisfied by the above and ‘‘ $n\delta x$ ’’ is the effective geometric radius of a test particle. We choose two sets of parameters, $n=1, \delta x=1.50$ fm; and $n=2, \delta x=0.75$ fm. These are listed in Table II. Often, when one wishes to simulate interactions of heavy ions the TPV method is employed, and one utilizes a finite configuration space grid. One then resolves the test particles up to some Euler grid scale and then assumes the validity of the TPV equations. This is clearly not correct and as we shall see leads to violation of energy conservation which can be quite extreme in some cases. Since this is a popular method, we too will artificially smooth the configuration space and introduce a non zero lattice constant when solving for TPV. One important aspect which differentiates the two methods is intimately connected with the two sets of equations of motion used. In particular the LHV equations of motion depend explicitly on the exact positions of all the particles within the cells. On the other hand, in the TPV method the test particles are only resolved up to a cell constant.

Note that the lattice Hamiltonian method with a MDYI-type momentum-dependent nuclear potential has been previously used by us in the context of nuclear flow inversion [25].

III. GROUND STATE NUCLEI

The first step in simulating a collision between two heavy ions is to initialize the ground state or starting position of the two nuclei. We should thus be able to approximately reproduce the binding energy per nucleon inside a nucleus. In introducing the nuclear matter potential in the previous section we have neglected two ingredients of the mean field that are important for practical applications. The first is the long range Coulomb potential and the second is the symmetry energy which we call here the isospin potential. With these, the potential energy density should read:

$$V_\alpha = V_\alpha^{nuc} + V_\alpha^{coul} + V_\alpha^{iso} \quad (3.1)$$

Here, V_α^{nuc} can be the MDYI potential from the previous section or any other potential one wishes to consider. The Coulomb potential takes its usual form and for the isospin, we adopt a form for the single particle potential previously used [26,27] which has the following potential energy density:

$$V_\alpha^{iso} = \frac{D}{2\rho_0}(\rho_\alpha^n - \rho_\alpha^p)^2 \quad (3.2)$$

The single particle potential is obtained by writing $U_\alpha^n \equiv \partial V_\alpha^{iso} / \partial \rho_\alpha^n$ for neutrons and the same with p replacing n for protons. In the above, $\rho_\alpha^n(\rho_\alpha^p)$ is the neutron(proton) density at grid site α . We will also consider one more potential which is a simplified version of the MDYI potential in which any momentum dependence is suppressed. We refer to this potential as ‘‘H’’ with a compressibility of $K=380$ MeV (see Table I). For detailed comparisons of these and other mean field potentials as far as flow observables are concerned, the reader is referred to [7].

The initialization of the test particles in phase space is done following usual techniques [5]. Using the two parameter sets described in the previous section, the binding energy per nucleon was calculated for nuclei in the mass range $A : 4 \rightarrow 208$. We find the difference between TPV and LHV to be negligible for a momentum-independent potential. For this case very good agreement is obtained with the Weizsäcker semi-empirical mass formula over the entire mass range studied. Parameter set II ($\delta x = 0.75$ fm) deviated by no more than about 0.5 MeV from the mass formula. Parameter set I consistently gave about 1 MeV larger binding energy per nucleon. For the momentum-dependent case however, both TPV parameter sets deviated substantially from the binding energy curve for $A < 20$, giving up to 8 MeV per nucleon too large a binding energy. Only parameter set I approached the binding energy curve at large A . Parameter set II gave too little a binding energy per nucleon (~ 6 MeV) for $A = 208$. For the LHV method, the shape of the binding energy curve was reproduced for both parameter sets, however parameter set I gave too large a binding energy per nucleon for low mass nuclei (~ 10 MeV for $A = 10$). Parameter set II performed well, only giving $\sim 0.5 \rightarrow 1$ MeV more binding than the mass formula.

Recently, it has been shown that the presence of a ‘‘neutron skin’’ should be taken into account in low energy heavy ion collisions [28,29]. Furthermore, if we wish to reproduce as well as possible the nuclear ground state it is desirable to be able to reproduce a neutron skin. A recent relativistic mean field calculation by Warda [32] has given a parameterization of the neutron and proton radii in heavy nuclei ($A > 60$). We used this parameterization to specify the initial neutron and proton radii. For nuclei with mass numbers smaller than $A=60$ we used the method employed by Sobotka [29] to generate neutron skins.

Another test for ensuring a close approximation to ground state nuclei is the nuclear stability as a function of time. The total energy per nucleon for a small (^{20}Ne) and a large (^{208}Pb) nucleus with the two parameter sets for the lattice spacing/form factors was investigated. The results are displayed in Figs. 1 and 2. From these figures, one sees that the TPV method suffers from an energy gain for both $n=1$ and $n=2$ (~ 2.5 (1.6) MeV/nucleon at $t=100$ fm/c for $n=1$ (2)) for the heavy Pb nucleus. Note that the energy gain is less severe for $n=2$ as well as for the heavier nucleus with a momentum-independent potential,

see Fig. 1. On the other hand, the LHV method shows that energy conservation is almost complete (gain of ~ 10 (30) KeV/A at $t=100$ fm/c for $n=1$ (2)) for both parameter sets. When we turn to the momentum-dependent case we see the drastic difference between the two parameter sets in the TPV method. Both suffer from energy nonconservation (~ 6.5 (71) MeV/nucleon at $t=100$ fm/c for $n=1$ (2)), however, for $n=2$, $\delta x=0.75$ fm (double line), the nucleus is highly unstable and quickly gains energy. The LHV method on the other hand shows only a very slight energy gain (~ 730 (860) KeV/A at $t=100$ fm/c for $n=1$ (2), respectively). The numbers above are summarized in Table III. We find that the amount of energy nonconservation is strongly dependent upon N_{ens} in the TPV method whereas the LHV method shows only a slight dependence on N_{ens} . This is illustrated in Fig. 3. For this reason alone, it is safer to use the LHV solution as any dependence on N_{ens} as seen in the TPV case is in some sense spurious. Note that we could in theory (and practice) push the limits of the TPV method by greatly increasing N_{ens} .

All calculations so far have been done on a finite configuration space grid. It is well known that calculations of these type generally break Galilean invariance and thus do not strictly conserve momenta [30]. In short, a “lattice friction” is generated, leading to momentum nonconservation. We have investigated this phenomena for a single ^{40}Ca nucleus moving with lab energies $E_k/A: 25 \rightarrow 200$ MeV. At each value of the bombarding energy, the nucleus was allowed to traverse the grid. The momentum conservation results for both momentum-independent and momentum-dependent mean fields in the TPV and LHV methods for both parameter sets are displayed in Fig. 4. From these figures we see that when $n=1$, the LHV method (dotted line) is more susceptible to lattice friction than the TPV method (solid line) for all studied potentials. The vulnerability of the LHV to lattice friction had been previously observed [22]. For $n=2$ the LHV (dashed line) and TPV (double line) give comparable results with a momentum-independent potential. The $n=2$ TPV fails with the momentum-dependent interaction. Both panels of this figure show that the relative momenta loss increases as the bombarding energy decreases. The kinks at low energy are due to fluctuations. In the next section we will specify which parameter set we shall use with a given potential, for optimal results in energy and momentum conservation.

IV. NUCLEAR COLLISIONS IN THE VLASOV LIMIT

The last sections elucidated the differences between the TPV and LHV approach for the initial as well as the time evolved state of a single nucleus. However, in heavy ion physics, it is the *interaction* of two nuclei that is of interest. So now the question arises as to how the two methods differ when we are dealing with a system of colliding nuclei. For the moment we are concerned with the integrity of the mean field and we need only consider the Vlasov limit of our model: we presently neglect hard nucleon-nucleon scattering (see next section). We have investigated the time evolution of the total centre of mass energy of a light ($^{20}\text{Ne}+^{20}\text{Ne}$) and a heavy ($^{208}\text{Pb}+^{208}\text{Pb}$) system, at bombarding energies from 25 MeV/nucleon to 400 MeV/nucleon. Both momentum-independent and momentum-dependent nuclear mean fields were considered. We found effects similar to that which were observed when considering only a single nucleus. Namely, TPV suffers from energy nonconservation for both parameter sets ($n=1$ and $n=2$), while the LHV method is much more stable (see below). The collisions considered here were at zero impact parameter.

We will report on the net energy change at different incident lab bombarding energies for the symmetric Pb system with a momentum-dependent mean field potential. For all cases, the energy variations increase as the beam energy decreases. For the LHV cases ($n = 1$ and 2) no more than ~ 1 MeV/nucleon was gained in the entire simulations at $E_k/A = 50$ MeV. This compares to ~ 9 MeV/nucleon for TPV ($n=1$) and ~ 80 MeV/nucleon for TPV ($n=2$). In general, the LHV method does a much better job of conserving energy. Indeed, for the better TPV case the energy gain is already comparable to the binding energy per nucleon. At kinetic energies per nucleon of around 200 MeV and higher, LHV yields a total energy variation less than 0.3 MeV/nucleon.

In summary of this section and of the previous one, the TPV method is satisfactory only with parameter set I for momentum-dependent potentials. The LHV method performs quite well with both momentum-independent and well as momentum-dependent potentials in terms of energy conservation, but parameter set I suffers from lattice friction. For these reasons, we will only consider from here on the TPV method with parameter set I and the LHV method with parameter set II (see Table I).

V. THE INCLUSION OF HARD SCATTERING

So far we have discussed differences arising in the TPV and LHV methods that affect the evolution of the mean field for both single and interacting nuclei. Individual nucleons can also collide with each other (*i.e.* undergo “hard scattering”). In order to include the hard scattering effects we require *a priori* the nucleon-nucleon scattering cross section. In this work we will consider only elastic collisions. A recent parameterization of the nucleon-nucleon cross section which includes isospin has been given by Cugnon, L’Hôte and Vandermeulen [33]. This cross section is an improvement over previous parameterizations [34] which have been used in BUU [7,5] and QMD [35,36] calculations. We present this cross section in Figure 5. From this figure one sees that the isospin asymmetric channel can be as large as 2.4 times the isospin symmetric channels. We also note that for collisions with kinetic energy equal to or smaller than $E_k^{\text{cm}} \sim 10$ MeV, the scattering cross section has been set to a constant value of 150 mb. We find that Pauli blocking of the final states prohibits the majority ($> 99\%$) of collisions with centre of mass energies below this value at the bombarding energies under study here. The energy integrated Pauli blocking efficiency for both light and heavy ground state nuclei is found to be $\sim 95\%$.

It is well known that the inclusion of hard scattering within the framework of a momentum-dependent mean field potential can introduce energy nonconservation [37]. In addition, the inclusion of nucleon-nucleon collisions tends to stop colliding nuclei (nucleons from both nuclei tend to pile up around the interaction zone). Thus, the properties of the mean field and those of collisions add up nonlinearly. This will be important for our comparisons of TPV and LHV since it has already been shown that TPV does not properly handle the mean field. For these reasons, we will reexamine energy conservation in collisions of nuclei in both the TPV and LHV methods this time with hard nucleon-nucleon scattering present. Note that these “new” comparisons will be renamed TPB (test-particle-Boltzmann) and LHB (lattice-Hamiltonian-Boltzmann). Figure 6 shows the growth of total centre of mass energy with two colliding Pb nuclei at $E_k/A = 100$ MeV. From this we see that both the TPB and LHB method now suffer from energy nonconservation. However, the

difference is that the energy gain in LHB is predominantly from collisions, while the energy non-conservation in TPB is from both collisions and mean field effects.

Using MDYI we note that with the TPB method, as the bombarding energy per nucleon decreases down to some critical value (~ 100 MeV), the total energy gain also decreases. Below this critical bombarding energy, the system suffers from an energy gain which is very roughly inversely proportional to the lab bombarding energy. Indeed, at low E_k , the energy gain per nucleon grows as E_k decreases and can be ≈ 6 MeV for a system of colliding Pb nuclei at $E_k/A = 50$ MeV. Since the hard nucleon-nucleon collisions and the mean field interact highly nonlinearly it is difficult to clearly isolate the cause of the energy gain. However, we do know that it should come mostly from the mean field propagation as most nucleon-nucleon collisions are Pauli blocked. With LHB, on the other hand, the total energy gain gradually decreases with decreasing E_k and eventually levels-off to the energy gain seen in Vlasov solutions (*i.e.* in LHV). This is just what one would again expect from Pauli blocking. For the practical application we have in mind in this work, we deem the energy conservation of the LHB solution satisfactory: for Pb + Pb at 50 MeV/nucleon, we only gain ≈ 1 MeV/nucleon.

VI. DATA COMPARISON

In this section we perform several comparisons of the TPB/LHB results with recent experimental measurements on nuclear stopping. The experiment was performed at the Michigan State University K1200 cyclotron and consisted of bombarding beams of ^{40}Ar on targets of Cu, Ag and Au. The beam energy per nucleon was in the range $8 \rightarrow 115$ MeV. A portion of this experiment involved identifying the heavy final state remnant's mass and velocity. The ratio v_{\parallel}/v_{cm} measured in the lab frame represents the stopping power of the above nuclear reactions. The ratio $v_{\parallel}/v_{cm} \sim 1$ indicates large stopping and partial nuclear fusion while the ratio $v_{\parallel}/v_{cm} \sim 0$ indicates less stopping. Here, v_{\parallel} is the longitudinal velocity of the heavy remnant in the lab frame and v_{cm} is the velocity of the centre of mass of the projectile + target system in the lab frame.

Before we discuss the comparisons we will first describe some relevant details of the simulations. We generated the nuclei with neutron and proton radii given by the methods of Warda [32] and Sobotka [29]. Note that the asymmetry parameter for Ar is small so we do not get a significant skin for this nucleus. The gold nucleus on the other hand has a large asymmetry parameter, thus the inclusion of a neutron skin is desirable. Next, the nuclei were boosted towards each other on Rutherford trajectories at the appropriate beam energy. The simulations were run until a single large remnant was well separated from all other "fragments". Simulation times ranged from $t: 325 \rightarrow 225$ fm/c for $E_k/A: 20 \rightarrow 120$ MeV, respectively. The next step in identifying the remnant was achieved by calculating the single particle total energy in a local rest frame. See reference [38], for example. A nucleon within the vicinity of the centroid of the large remnant was considered bound to this remnant only if the total energy of the nucleon in a local rest frame was negative. This allowed for a nice identification of the heavy remnant as we shall see. Finally, the total mass and lab frame velocity was then deduced from this remnant.

We considered in turn the momentum-independent and momentum-dependent potentials discussed in this work. Furthermore, a second momentum-dependent potential was consid-

ered here. We refer to this potential as GBD. Details can be found in reference [7]. We find that the energy and momentum conservation with this potential to be similar to that found in the MDYI investigations of the previous sections. The potential energy density for this potential reads as follows (see also Table I):

$$V(\vec{r}) = \frac{A}{2} \frac{\rho(\vec{r})^2}{\rho_0} + \frac{B}{\sigma + 1} \frac{\rho(\vec{r})^{\sigma+1}}{\rho_0^\sigma} + \frac{C\Lambda^2 \rho(\vec{r})}{\rho_0} \int d^3p \frac{f(\vec{r}, \vec{p})}{\Lambda^2 + (\vec{p} - \langle \vec{p} \rangle)^2}. \quad (6.1)$$

Figure 7 shows the results from the MSU experiment as well as the TPB/LHB simulations for three different nuclear potentials. The momentum-independent potential referred to as “H” has a compressibility of $K=380$ MeV. Both the GBD and MDYI potentials have compressibilities of $K=215$ MeV. The experimental multiplicity gate corresponds to an impact parameter $b \sim b_{max}/4$ [39]. The simulations were run for two impact parameters of $b=b_{max}/3$ and $b=b_{max}/5$ in an attempt to bracket the data.

Let us first consider the TPB momentum-independent calculations. We see from the figure that the remnant masses are reproduced within experimental uncertainty. On the other hand, the LHB result indicates that the trend is reproduced but the magnitude is slightly overestimated at low E_k . One might be tempted to naively assume that the larger mass seen in LHB (over that of TPB) can be attributed to the energy gain (*i.e.* increased nucleon evaporation) in TPB which is absent in LHB. However, when we turn to the momentum-dependent results (GBD) it is clear that this is not the case there. The TPB results again underestimate the remnant mass and roughly reproduce the data trend. LHB on the other hand reproduces neither the trend nor the magnitude of the data. The GBD/LHB result shows that the remnant mass drops rapidly for incident energies $E_k/A : 20 \rightarrow 60$ MeV and settles onto a plateau above 60 MeV. Here, the remnant masses are quite low ($A < 25$). In fact, it is observed that the GBD/LHB final state consisted of many small and equally sized remnants. As we shall see, this leads to difficulties in determining the remnant velocity as it is unclear which fragment represents the “large” remnant. Finally, the MDYI/TPB result is similar to GBD/TPB (*i.e.* magnitude underestimated). On the other hand, the MDYI/LHB result shows much better agreement with the data trend and only slightly underestimates the remnant mass. From the figure it is clear that the momentum-independent TPB gives the best overall agreement with the data. For the momentum-dependent result, the best agreement is obtained with MDYI/LHB.

Next we turn to the remnant velocity distributions. Figure 8 shows the experimental and calculated results for the three potentials and two methods discussed previously. We see from this figure that the momentum-independent calculations fail to reproduce the data for both TPB and LHB. In fact, for all three potentials the TPB results do not reproduce the data. However, we have better agreement with a momentum-dependent potential. When we turn to the LHB momentum-dependent results, it is observed that the GBD potential just brackets the data. In fact for $b = b_{max}/3$, the data is reproduced quite well. The MDYI also does a better job than the momentum-independent potential, especially at the larger impact parameter. However the agreement is not as good as with the GBD potential. Note the large error bars seen in the GBD/LHB calculation. This follows from the ambiguity encountered in determining the large final state remnant discussed in the previous paragraph, this difficulty is absent in the calculations done using other interactions.

VII. CONCLUSION

In summary, we see agreement with the measured remnant mass obtained with the LHB method, except with the GBD potential. This potential gives poor agreement with this data. Both the momentum-independent and MDYI potentials give good agreement with the data. For the velocity distributions, the TPB method failed for all three potentials. Reasonable agreement could be achieved only with a momentum-dependent potential in the LHB method. Overall it appears that the MDYI interaction, used with the Lattice Hamiltonian algorithm achieves a satisfactory general description of the experimental data. Coupled with the reasonable ground state solutions of this combination and with the fact that the MDYI receives support from higher energy flow data [7], this situation is satisfying. Further note that a hard momentum-dependent interaction does not seem to be supported by the higher energy data, nor by the data discussed in this work [41].

We are now in a position to consider other observables such as the balance energy and also to try and extract information on possible in-medium variations of the nucleon-nucleon cross sections. Those issues are under investigation. By now it is clear that progress in the theoretical study of heavy ion collisions can only be achieved through the simultaneous investigation of a collection of related physical observables.

ACKNOWLEDGMENTS

We are happy to acknowledge useful discussions with P. Danielewicz, S. Das Gupta, and R. Lacey. This work is supported in part by the National Science and Engineering Research Council of Canada and in part by the Fonds FCAR of the Québec government. One of us (D.P.) is happy to acknowledge the financial support of McGill University through the Alexander McFee Memorial Fellowship.

REFERENCES

- [1] See, for example, Hildegard Meyer-Ortmanns, *Rev. Mod. Phys.* **68**, 474 (1996), and references therein.
- [2] See *Proceedings of the Sixth International Conference on Nucleus-Nucleus Collisions*, *Nucl. Phys.* **A 629** (1998), and references therein.
- [3] See, for example, Madappa Prakash, Ignazio Bombaci, Manju Prakash, Paul J. Ellis, James M. Lattimer, and Rolland Knorren, *Phys. Rep.* **280**, 1 (1997), and references therein.
- [4] J.P. Blaizot, D. Gogny, and B. Grammaticos, *Nucl. Phys.* **A 265**, 315 (1976).
- [5] G.F. Bertsch and S. Das Gupta, *Phys. Rep.* **160**, 189 (1988).
- [6] G.M. Welke, M. Prakash, T.T.S. Kuo, S. Das Gupta and C. Gale, *Phys. Rev. C* **38**, 2101 (1988).
- [7] J. Zhang, S. Das Gupta and C. Gale, *Phys. Rev. C* **50**, 1617 (1994).
- [8] P. Danielewicz and G. Odyniec, *Phys. Lett.* **B 157**, 146 (1985).
- [9] H.H. Gutbrod, A.M. Poskanzer, and H.G. Ritter, *Rep. Prog. Phys.* **52**, 1267 (1989).
- [10] M.D. Partlan, *Phys. Rev. Lett.* **75**, 2100 (1995).
- [11] F. Haddad *et. al.*, *Phys. Rev. C* **52**, 2013 (1995).
- [12] J. P. Blaizot, J. F. Berger, J. Dechargé, and M. Giroto, *Nucl. Phys.* **A591**, 435 (1995); M. Farine, J. M. Pearson, and F. Tondeur, *Nucl. Phys.* **A615**, 135 (1997).
- [13] D. H. Youngblood, H. L. Clark, and Y.-W. Lui, *Phys. Rev. Lett.* **82**, 691 (1999).
- [14] G.D. Westfall *et. al.*, *Phys. Rev. Lett.* **71**, 1986 (1993).
- [15] D. Klakow, G. Welke and W. Bauer, *Phys. Rev. C* **48**, 1982 (1993).
- [16] A. Hombach, W. Cassing and U. Mosel, *Eur. Phys. J.* **A5**, 77 (1999).
- [17] V. de la Mota, F. Seville, M. Farine, B. Remaud, and P. Schuck, *Phys. Rev. C* **46**, 677 (1992).
- [18] B. Friedman and V.R. Pandharipande, *Phys. Lett.* **B 100**, 205 (1981).
- [19] R. Maffiet, *Prog. Part. Nucl. Phys.* **21**, 207 (1988).
- [20] See, for example, J.P. Jeukenne, A. Lejeune and C. Mahaux, *Phys. Rep.* **25C**, 83 (1976), and references therein.
- [21] See, for example, László P. Csernai, George Fai, Charles Gale and Eivind Osnes, *Phys. Rev. C* **46**, 736 (1992), and references therein.
- [22] R.J. Lenk and V.R. Pandharipande, *Phys. Rev. C* **39**, 2242 (1989).
- [23] C. Gale *et. al.*, *Phys. Rev. C* **41**, 1545 (1990).
- [24] See, for example, John W. Negele and Henri Orland, *Quantum Many-Particle Systems* (Addison-Wesley, Redwood City, 1988).
- [25] D. Persram and C. Gale in: *AIP conference proceedings: Toward the Theory of Everything: MRST '98*, eds. J.M. Cline, M.E. Knutt, G.D. Mahlon and G.D. Moore (AIP, Woodbury, New York, 1998) p.227
- [26] M.B. Tsang *et. al.*, *Phys. Rev. C* **40**, 1685 (1989).
- [27] Bao-An Li and Sherry J. Yennello, *Phys. Rev. C* **52**, R1746 (1995).
- [28] Bao-An Li, ZhongZhou Ren, C.M. Ko and Sherry J. Yennello, *Phys. Rev. Lett.* **76**, 4492 (1996).
- [29] L.G. Sobotka, *Phys. Rev. C* **50**, R1272 (1994).
- [30] M.P. Allen and D.J. Tildesley, *Computer Simulations of Liquids*. Oxford Science Publications, (1996).

- [31] R. Pak et. al., Phys. Rev. Lett. **78**, 1026 (1997).
- [32] M. Warda, B. Nerlo-Pomorska and K. Pomorski, Nucl. Phys. **A635**, 484 (1998).
- [33] J. Cugnon, D. L'Hôte and J. Vandermeulen, NIM **B111**, 215 (1995).
- [34] J. Cugnon, T. Mizutani and J. Vandermeulen, Nucl. Phys. **A352** 505(1981).
- [35] J. Aichelin and H. Stöcker, Phys. Lett **B176**, 14(1986).
- [36] J. Aichelin, Phys. Rep. **202**, 233 (1991).
- [37] C. Gale and S. Das Gupta, Phys. Rev. C **42**, 1577 (1990).
- [38] Qiubao Pan and Pawel Danielewicz, Phys. Rev. Lett. **70**,2062 (1993).
- [39] R. Sun *et. al.*, Stony Brook preprint, 1998.
- [40] R. Sun, private communication.
- [41] Declan Persram and Charles Gale, *Proceedings of MRST '99: High Energy Physics at the Millenium*, nucl-th/9907068.

TABLES

TABLE I. Parameters for nuclear matter potentials considered in this work. All entries have units of MeV except σ and m^*/m , which are pure numbers.

potential	A	B	σ	C	Λ	m^*/m	$U(\rho_0, p_f)$	$U(\rho_0, 0)$	$U(\rho_0, \infty)$	K
H	-124.0	70.5	2.0	-	-	1	-53.5	-53.5	-53.5	380
GBD	-144.0	203.3	7/6	-75.0	400.0	0.7	-53.3	-76.3	-1.34	215
MDYI	-110.4	140.9	1.24	-64.95	415.7	0.67	-52.9	-75	30.5	215

TABLE II. Parameter sets used for the single-particle equations of motion.

parameter set	n	$\delta x [fm]$	N_{ens}
I	1	1.50	100
II	2	0.75	25

TABLE III. Energy gain for a single Pb nucleus after $t = 100$ fm/c. All entries have units of MeV.

parameter set	$\Delta E [MeV]$			
	TPV		LHV	
	mom.ind.	mom.dep.	mom.ind.	mom.dep.
I	2.5	6.5	0.01	0.73
II	1.6	71	0.03	0.86

FIGURES

FIG. 1. Time evolution of the total energy per nucleon in ^{20}Ne and ^{208}Pb for a momentum-independent ($K=380$ MeV) nuclear mean field. The results for four distinct calculations are shown. Coulomb and Isospin effects are included in the mean field. The following situations were considered: TPV [$n = 1, \delta x = 1.5$ fm] (solid line), TPV [$n = 2, \delta x = 0.75$ fm] (double line), LHV [$n = 1, \delta x = 1.5$ fm] (dotted line), and LHV [$n = 2, \delta x = 0.75$ fm] (dashed line).

FIG. 2. Same as figure 1 but with a momentum-dependent mean field. The momentum dependence used here is of the MDYI type with a compressibility of $K=215$ MeV.

FIG. 3. Energy gain for a single Pb nucleus in the TPV and LHV methods. The energy gain is plotted as a function of N_{ens} . Both parameter sets considered in this work are shown and all calculations here are for the MDYI momentum-dependent mean field potential including Coulomb and isospin effects. The energy gain is after 100 fm/c. Note that due to the large time required for the momentum-dependent LHV simulation with $N_{ens} = 200$, that data point is not shown. All lines have the same meaning as those in figure 1.

FIG. 4. Percentage of lost forward momenta for a single ^{40}Ca nucleus moving at lab energies of $E_k/A : 25 \rightarrow 200$ MeV. The results obtained with a momentum-independent ($K=380$ MeV) and a momentum-dependent (MDYI, $K=215$ MeV) nuclear mean field are shown in the left and right panel, respectively. Note that for the momentum-dependent case, the TPV solution with $n=2$ and $\delta x = 0.75$ fm (double line) suffers from an energy gain large enough to overwhelm lattice friction effects. All lines have the same meaning as those in figure 1.

FIG. 5. Parameterization of the free space isospin dependent elastic cross section used for binary $pp(nn)$ and np collisions. Note that the isospin asymmetric channel (np) can have a cross section of about 2.4 time the isospin symmetric channel (pp or nn). These parameterizations are taken from Ref. [33].

FIG. 6. Time evolution of the total energy per nucleon in the nucleus-nucleus centre of mass frame for $^{208}\text{Pb}+^{208}\text{Pb}$ collisions at a lab bombarding energy of 100 MeV/A. Coulomb and Isospin effects as well as hard nucleon-nucleon scattering have been included. The results shown are for a momentum-dependent MDYI nuclear mean field of compressibility $K=215$ MeV. The solid line is the TPB result and the dashed line is the LHB result.

FIG. 7. Mass number of the heavy remnant from experiment and the TPB(left panels) and LHB(right panels) simulations for the Ar+Ag system. The error bars on the calculated points are one standard deviation statistical errors. The error bars on the experimental points are about 10% the value of the data point [40]. The top two panels represent calculations with a momentum-independent potential. The middle two are with the GBD momentum-dependent interaction and the bottom two are with the MDYI momentum-dependent interaction.

FIG. 8. Experimental and calculated average velocity ratios of the heavy remnant from figure 7. The error bars on the calculated points are one standard deviation statistical errors. The error bars on the experimental points are about 10% the value of the data point [40]. All panels are as described in figure 7.

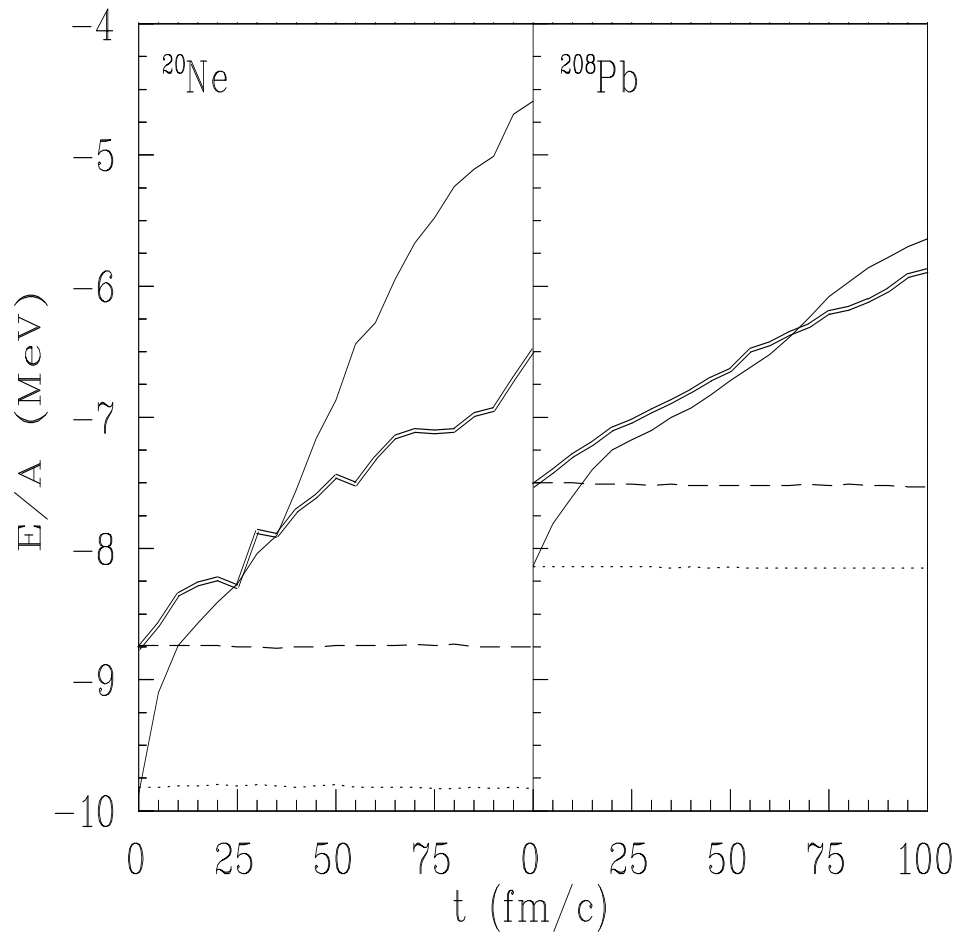


FIGURE 1.

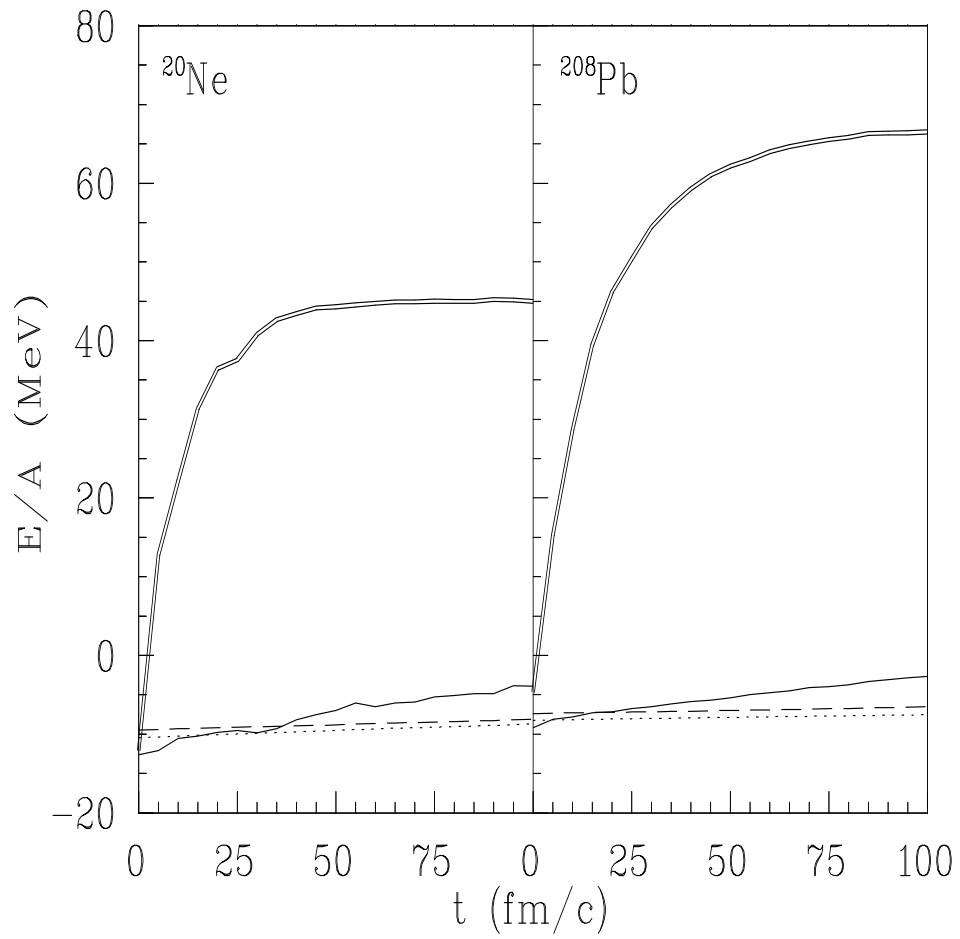


FIGURE 2.

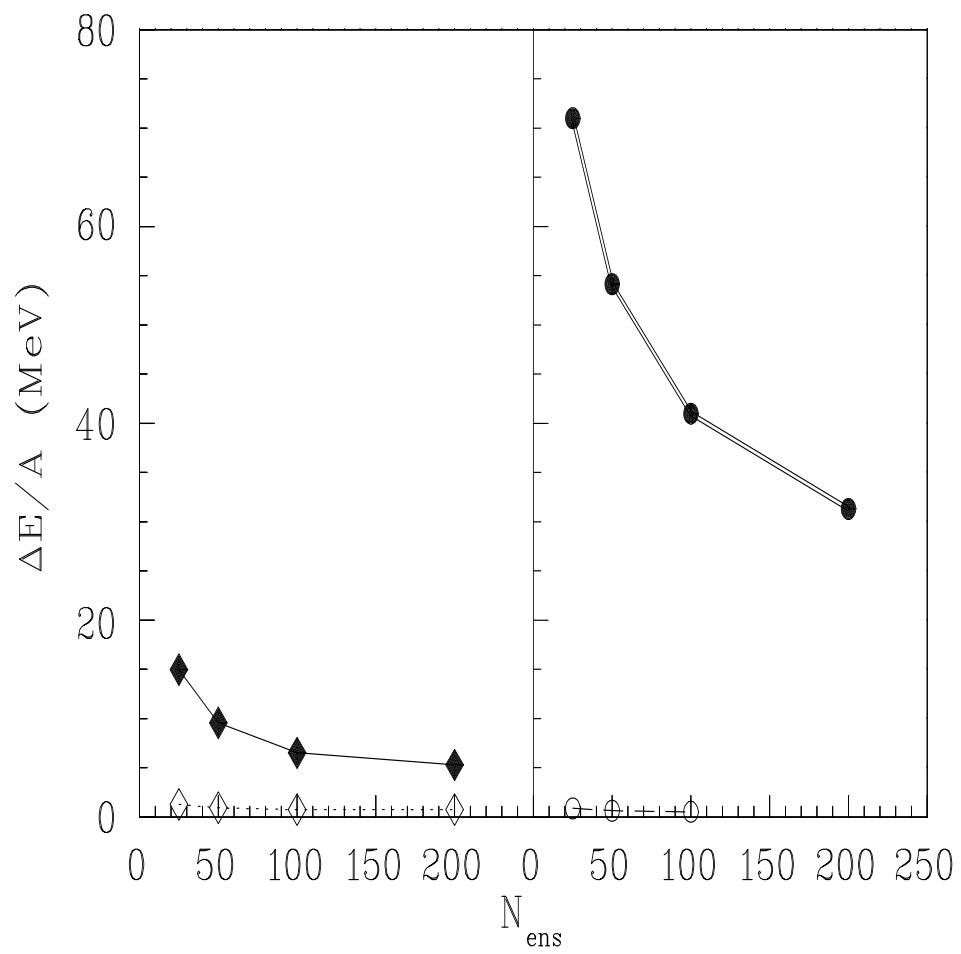


FIGURE 3.

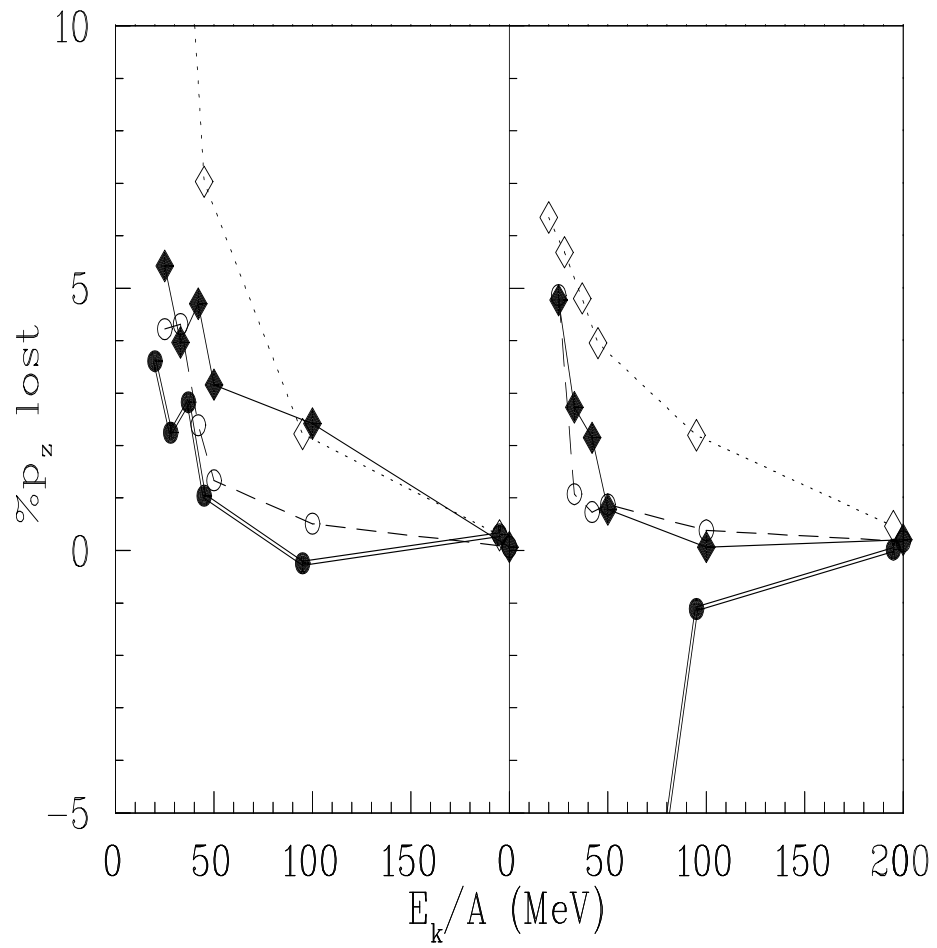


FIGURE 4.

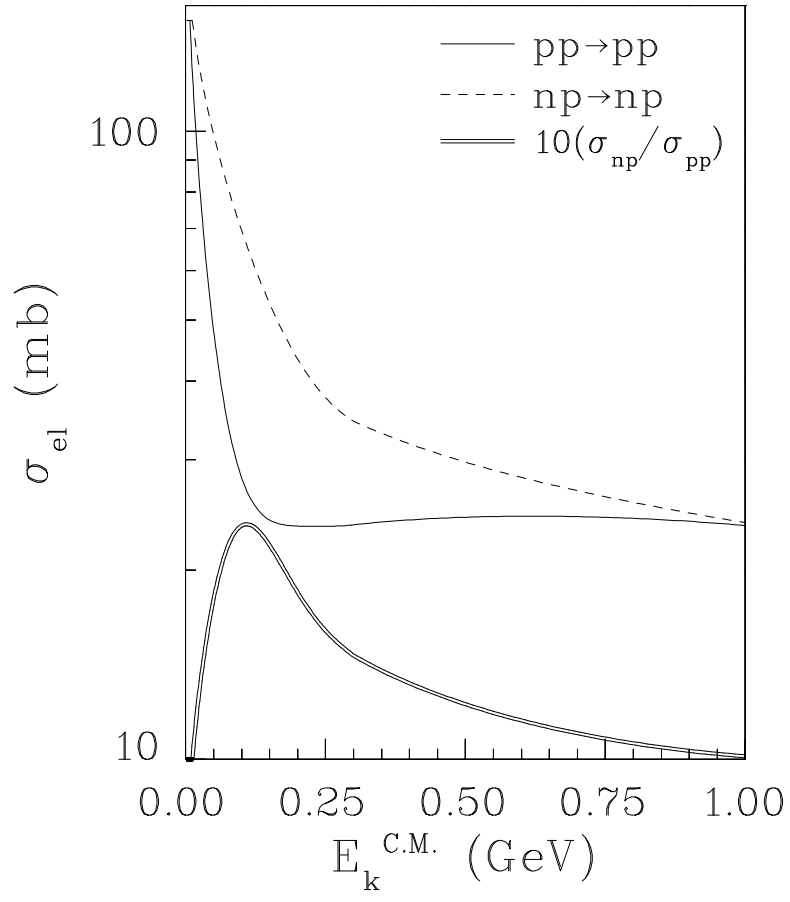


FIGURE 5.

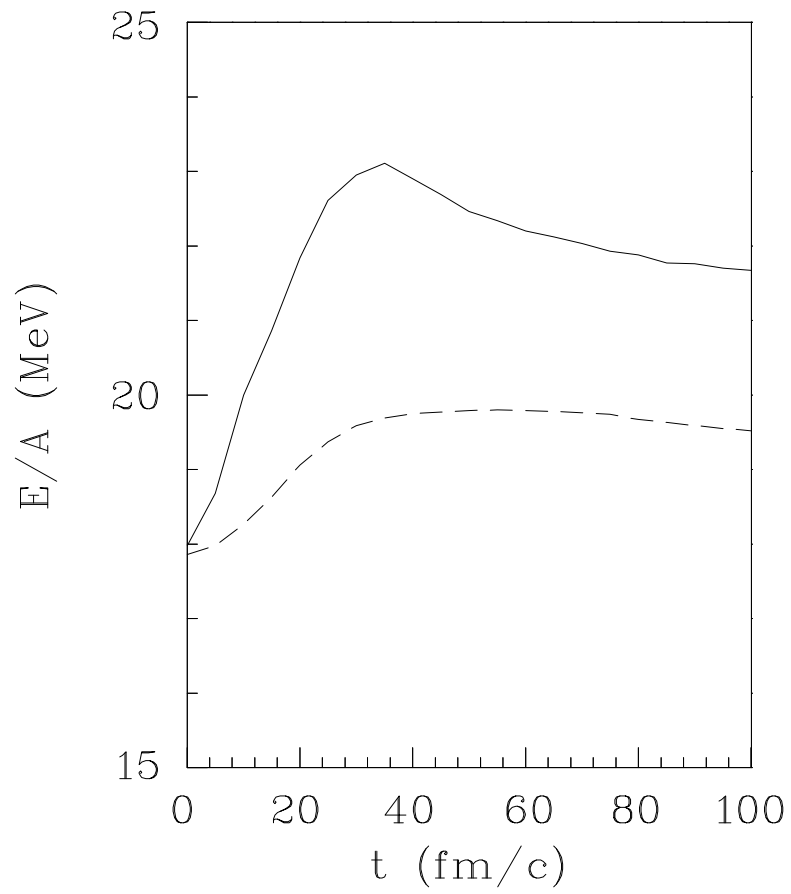


FIGURE 6.

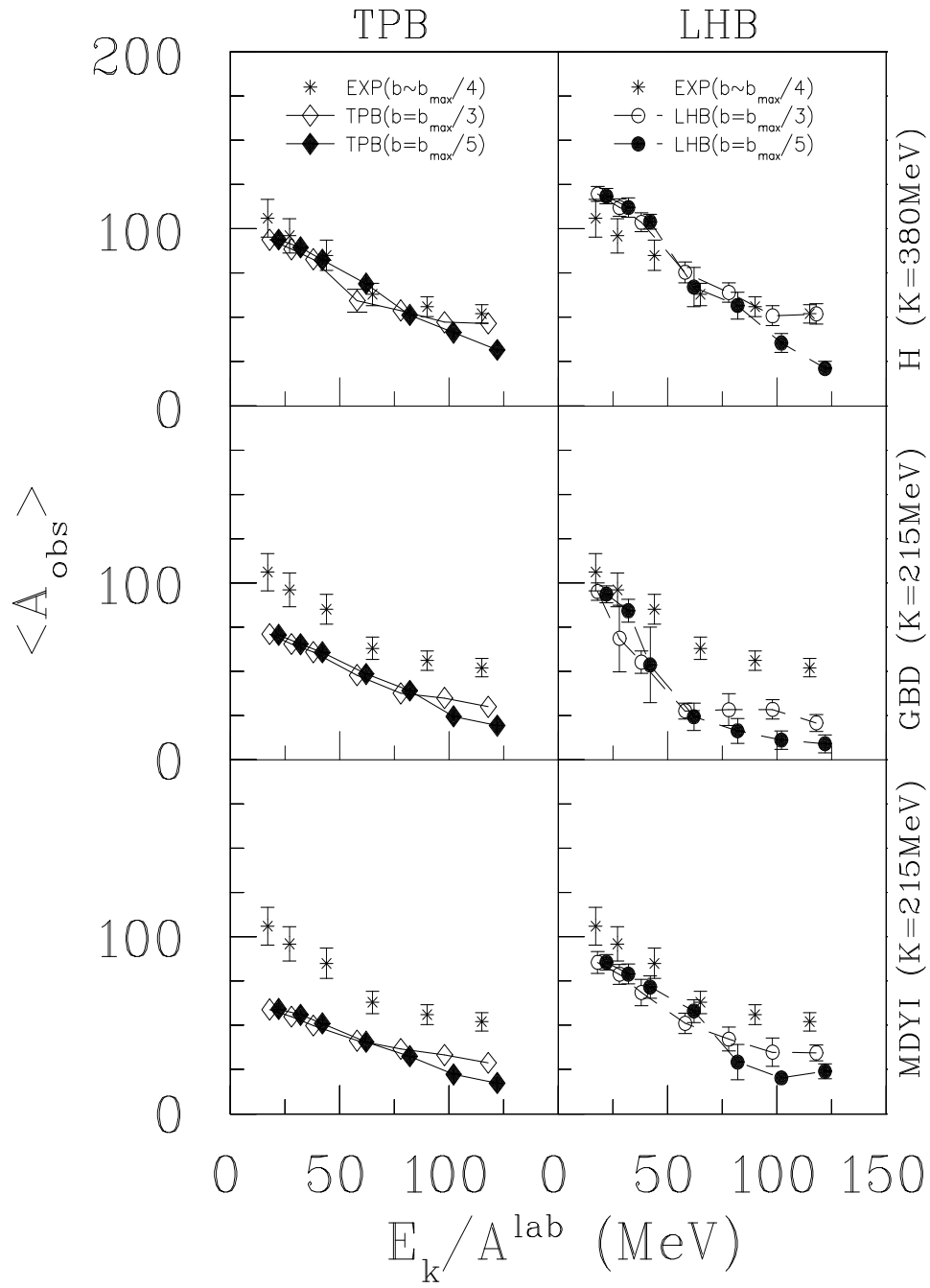


FIGURE 7.

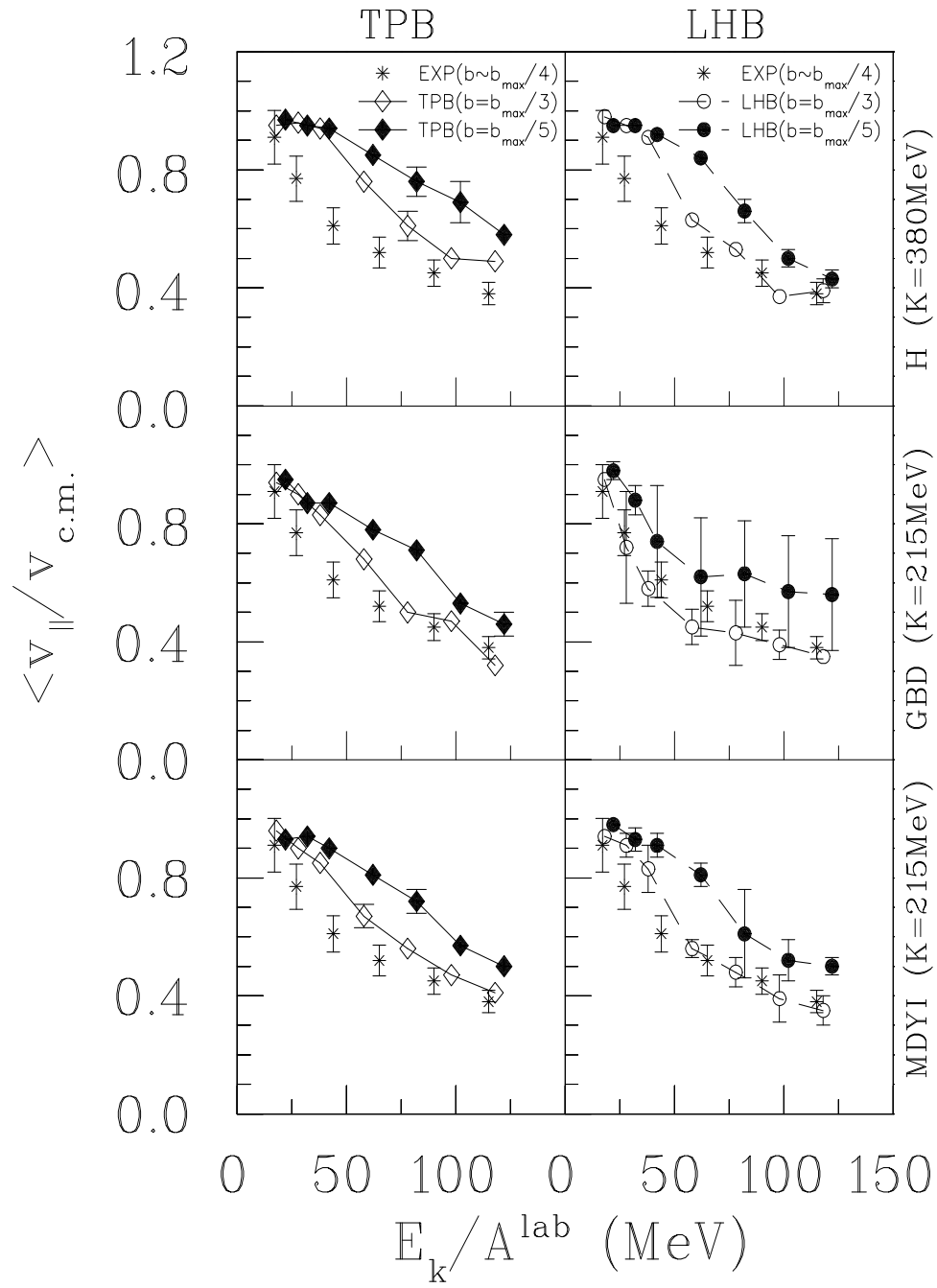


FIGURE 8.